ROYAL SOCIETY
OF CHEMISTRY

PAPER

Check for updates

Adsorption enhancement of nitrogen gas by atomically heterogeneous nanospace of boron nitride†

Jun Kimura,[a] Takahiro Ohkubo, [ID] *[a] Yuta Nishina, [ID] [b] Koki Urita [ID] [c] and Yasushige Kuroda [ID] [a]

In this study, porous boron nitride (p-BN) with hexagonal phase boron nitride (h-BN) pore walls was synthesized using high-temperature calcination. Negligible variation in pore-wall structure can be observed in powder X-ray diffraction (XRD) profiles and infrared (IR) spectra. However, a highly stable p-BN with a stable pore structure even at 973 K under the oxidative conditions is obtained when synthesized at higher than 1573 K under nitrogen gas flow. For p-BN, this stability is obtained by generating h-BN microcrystals. Nitrogen adsorption–desorption isotherms at 77 K provide type-IV features and typical adsorption–desorption hysteresis, which suggests micropore and mesopore formation. Moreover, adsorption–desorption isotherms of Ar at 87 K are measured and compared with those of nitrogen. The relative adsorbed amount of nitrogen (*i.e.*, the amount of nitrogen normalized by that of Ar at each relative pressure or adsorption potential value) on p-BN is considerably larger than that on microporous carbon at low-pressure regions, which suggests the existence of strong adsorption sites on the p-BN surface. In fact, the relative number of adsorbed nitrogen molecules to that of Ar on p-BN is, at most, 150%–200% larger than that on microporous carbon for the same adsorption potential state. Furthermore, additional adsorption enhancement to nitrogen between $P/P_0 = 10^{-5}$ and 10^{-3} can be observed for p-BN treated at 1673 K, which suggests the uniformly adsorbed layer formation of nitrogen molecules in the vicinity of a basal planar surface. Thus, unlike typical nanoporous sp^2 carbons, p-BN materials have the potential to enhance adsorption for certain gas species because of their unique surface state.

Introduction

Many studies have examined the latent and outstanding properties of nanoporous materials. This is because the nano-ordered space fabricated by solids can provide unprecedented states of restricted molecules and ions that cannot be observed in any bulk phases. Many properties stemming from the confinement of molecules and ions in such quite narrow space involve potential abilities to shed light on the way to solve many issues for research fields like energy storage, purification, and separation. Thus, porous materials are often examined because

of their excellent functions as adsorbents and catalysts. These materials include carbon nanotubes,[1,2] zeolites,[3] and metal–organic frameworks.[4–8] Their specific pore geometry and surface activities can generate distinct chemical properties.

The outstanding physical and chemical properties of boron nitride (BN) have been identified alongside carbon materials. Although a BN unit is isoelectronic with a carbon–carbon (*i.e.*, CC) unit and certain solid-phase forms of BN are similar to carbon structures, most of its properties, such as colour, electric conductivity, and oxidation reactions, are different. Due to these characteristic properties, studies to develop synthetic routes of BN have been attempted because of its difficulty in yielding large-sized crystals. For instance, wafer-scale 2D single crystals of hexagonal phase BN (h-BN) have been synthesized on the surface of metal species such as Cu to develop electronic devices.[9] In addition, anomalous BN materials have interesting properties. Studies have reported amorphous phase BN with a low dielectric constant.[10] Furthermore, studies suggest that catalytic reactions can be initiated on the BN surface.[11,12] Such unprecedented properties of BN have been led by lots of attempts to develop new synthetic routes.[13–15] Based on these efforts, porous BN (p-BN) materials have been identified as

[a]Department of Chemistry, Graduate School of Natural Science and Technology, Okayama University, 3-1-1 Tsushimanaka, Kita-ku, Okayama 700-8530, Japan. E-mail: ohkubo@okayama-u.ac.jp

[b]Research Core for Interdisciplinary Sciences, Okayama University, 3-1-1 Tsushimanaka, Kita-ku, Okayama 700-8530, Japan

[c]Graduate School of Engineering, Nagasaki University, 1-14 Bunkyo-machi, Nagasaki, Nagasaki 852-8521, Japan

† Electronic supplementary information (ESI) available: Materials, powder XRD profiles, IR spectra, high-resolution XPS spectra, wide-energy-range XPS spectra, N_2 adsorption–desorption isotherms, pore-size distributions, SEM images and relative adsorption amounts of N_2 to Ar on h-BN. See DOI: 10.1039/d0ra08437a

prominent porous materials because of their fascinating performances.[16–24] An interesting study was published by Shankar *et al.* who insisted that p-BN can adsorb a relatively large amount of CO_2 at room temperature and reduce CO_2 to CO under light-irradiated conditions.[25] Because of this information, it is evident that p-BN materials are promising as novel adsorbents and catalysts.

Gas adsorption data can be used to obtain the characteristics of solid materials. In particular, dinitrogen (N_2) adsorption isotherms at its boiling point temperature have been applied to identify surface and pore structure such as specific surface area, pore volume, and pore-size distribution (PSD). A number of researchers examined the surface and pore structure of solid materials by analysing the adsorption isotherms of N_2. In many cases, N_2 is the most probable candidate to determine the surface and pore structure because it is the most common gas species with minimal specific interactions for various types of solid materials. Indeed, for explaining surface and pore structure, minimal specific interaction between a gas molecule and a solid surface is indispensable. Furthermore, when the close-packed monolayer of the gas molecules is assumed to have formed, analytical values such as specific surface area can be resolved by the adsorbed amount. In addition to N_2, noble gases are the most suitable gas species for analysing solid materials, of which Ar is optimal because of its moderate polarizability, which ensures appropriate formation of surface monolayer. Furthermore, similar to N_2, Ar is relatively inexpensive. Actually, Neimark *et al.* reported that PSDs of some MCM-41-type adsorbents obtained by N_2 isotherms at 77 K are in good agreement with those obtained by Ar isotherms at 87 K.[26] The report strongly supports that it has no trouble on the selection between N_2 and Ar to analyse the pore structure of mesoporous silica materials. As a probe gas species for surface and pore analyses, Ar is not as popular as N_2; however, in some cases, it can provide more accurate values for specific surface area and pore volume.[27,28] This is because Ar is a monoatomic molecule that is perfectly spherical; it has no special interactions other than dispersion force. For analysing microporous carbon materials, the adsorption isotherms of Ar can provide more accurate parameters compared to N_2.[29] Accordingly, although N_2 is commonly used because of its simplicity in handling and procurement, it is not a perfect probe molecule for analysing specific surface area or pore structure. Especially, any solid materials having an atomically heterogeneous surface have a possibility to powerfully adsorb gas molecules other than noble gases due to a relatively stronger interaction than the dispersion force. In this study, we discuss the specific properties of p-BN for N_2 adsorption by comparing the experimental results of both Ar isotherms and microporous carbon adsorbents having the isoelectronic pore wall to BN.

Results and discussion

Structure and surface chemistry of porous boron nitride

Before examining the adsorption characteristics of p-BN, the fundamental features were elucidated such as structure and surface chemistry. Fig. 1 shows the powder X-ray diffraction (XRD) profiles of p-BN obtained at 1473, 1573, and 1673 K,
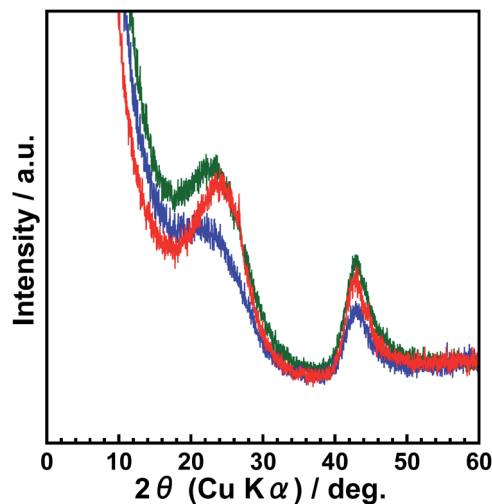

Fig. 1 Normalized powder XRD profiles of p-BN-1473 (green), p-BN-1573 (blue) and p-BN-1673 (red).

which are called p-BN-1473, p-BN-1573, and p-BN-1673, respectively. The profiles shown in Fig. 1 were normalized to fit the data of p-BN-1673 over $2\theta > 80°$. This procedure is based on the principle that X-ray scattering intensity can be normalized to electron units, which is a function of the total number of electrons in the material in question.[30] In other words, for the wide-angle region in XRD profiles, the scattering intensities of different samples with the same chemical composition can be standardized. In fact, Fig. 1 shows the normalized profiles, which were obtained from the raw data (Fig. S1, ESI†) by multiplying p-BN-1473 and p-BN-1573 by 0.94 and 1.12, respectively. All profiles have broad diffraction bands at (002) and (100) reflections,[21] indicating the formation of amorphous p-BN. Of these three samples, p-BN-1673 has the most ordered structure with respect to stacking and in-plane directions because of sharper (002) and (100) band profiles. In addition to XRD profiles, the formation of the BN framework is supported by infrared (IR) spectra. The IR spectra of all p-BN samples are identical, as shown in Fig. S2 (ESI).† The bands at ~1400 and 800 cm^{-1} can be assigned to the in-plane (E_{1u}) and out-of-plane (A_{2u}) modes of h-BN.[31] Thus, the synthesized compounds were entirely amorphous phase BN composed of h-BN microcrystals.

For better understanding of p-BN structure, we took high-resolution transmission electron microscopy (HR-TEM) and scanning transmission electron microscopy (STEM) images. The structural images of p-BN-1673 are shown in Fig. 2. The sample is constructed by curved sheets stacking a few layers and nanometre-scale pores formed in between the sheets as shown in Fig. 2a. Such pores are clearly observed in the STEM image depicted in Fig. 2b. Although micropores are hard to be observed due to its complicated and amorphous structure, mesopores are certainly formed. The disordering of the BN frameworks observed in the image is well consistent with the broadened (002) profile of p-BN-1673 in the XRD results shown in Fig. 1. The pore formation will be discussed in the latter section by using gas adsorption–desorption results.
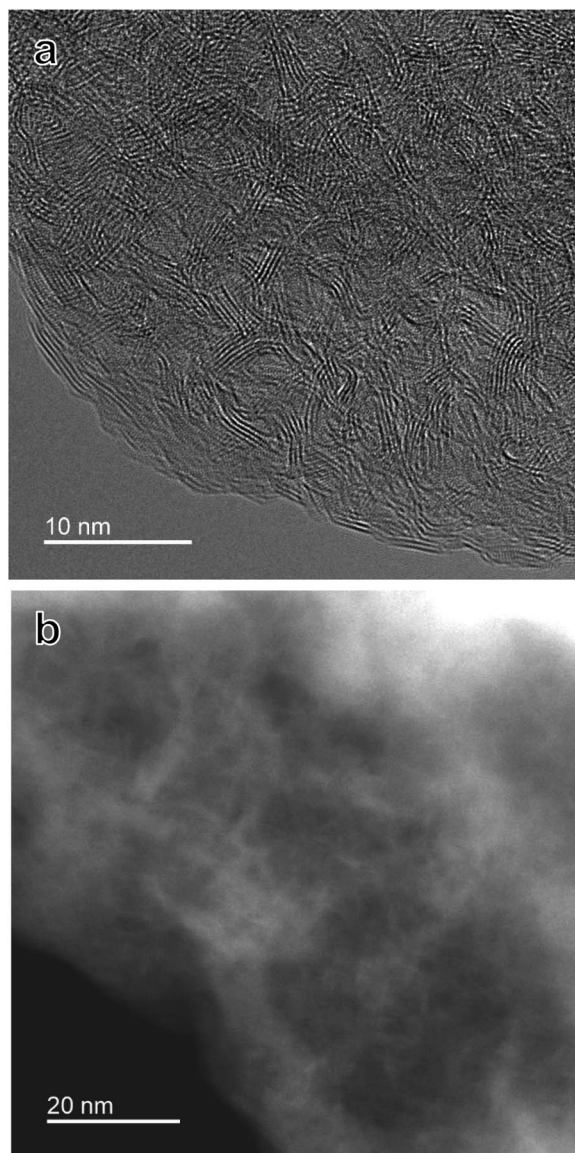
Fig. 2 (a) HR-TEM and (b) STEM images of p-BN-1673.

Fig. 3 TG curves of (a) p-BN-1473, (b) p-BN-1573, (c) p-BN-1673 and (d) h-BN.

Although the p-BN samples have similar structures, differences can be observed in the oxidation stability due to differences in surface chemistry. Fig. 3 shows thermogravimetric (TG) curves of p-BN and crystalline h-BN under atmospheric conditions. As expected, h-BN is stable against oxidation up to 1173 K because no deviations can be observed from the origin in the TG curve as shown in Fig. 3d. All TG curves for p-BN have similar inclinations: steep drop-off prior to 373 K followed by a gradual decline until a sharp increase to <1000 K. The decrease under 373 K and the sharp increase over 1000 K are considered as the desorption of pre-adsorbed water on p-BN and the oxidation process of the BN framework, respectively. Here, we can easily observe that the starting temperature of oxidation increases with increase in the heat-treatment temperature from 1473 to 1673 K. This suggests that the oxidation stability of the BN framework increases with an increase in the heat treatment temperature. As shown in Fig. S3 and S4 (ESI),† a boron oxide

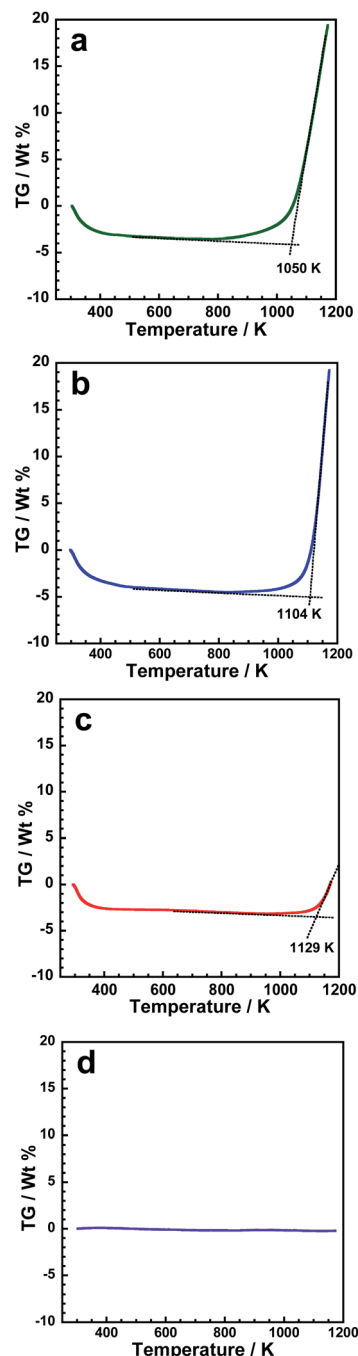species, B_2O_3, can be observed only for p-BN-1473 after oxidation at 973 K for 1 h in air, which is consistent with the TG results shown in Fig. 3. These results suggest that the synthesis temperature is directly linked to oxidation stability; the surface properties of the samples in question, such as chemical composition and local p-BN structure, are different although the overall structures derived by XRD and IR are similar.

Any differences in the surface chemical states can be explained by variation in the p-BN stability against oxidation. In

this study, we examined the surface chemistry of p-BN using XPS. Fig. 4 shows the B1s and N1s XPS spectra of both p-BN and h-BN. Although h-BN only has individual bands in the B1s spectrum, the B1s bands of p-BN are convoluted by three isolated species. These bands can then be assigned to B–C, B–N, and B–$O_x N_y$ species, as shown in Fig. 4a.[21,32] Moreover, apparent variation was detected in the relative band intensity assigned to B–C species; the band intensities increased with an increase in synthesis temperature. The variation in band intensity suggests that the carbon atoms originated by a precursor species of urea were impregnated into the h-BN microcrystals of p-BN. Such an impregnated state can be observed from the C1s XPS spectra

shown in Fig. S5 (ESI);† the band at ~282.0 eV, which can be assigned to carbide species, increased with an increase in synthesis temperature. Furthermore, the characteristic bands for N1s spectra can be observed, as shown in Fig. 4b. One of the p-BN bands detected at ~395.5 eV cannot be observed for the h-BN spectrum. This band can be assigned to nitride species, such as a metal nitride,[33] and is obviously larger for p-BN-1673 than those for p-BN-1473 and p-BN-1573. Characteristic bands can also be observed in the O1s XPS spectra of p-BN, as shown in Fig. S6 (ESI).† Although the band from B–OH formation can be observed at ~532.5 eV, it is in a lower energy region compared with h-BN (533.7 eV).[34] Furthermore, another characteristic band at ~529.0 eV can be observed, the position of which is typically assigned to a metallic oxide or a boron oxide.[35] Here, metal impurities might be deposited because certain bands are assigned to typical metal compounds such as metal nitride and metal oxide. Al is the most probable metal species for this contamination because alumina boat and tube were used in this study. If Al species were involved in the sample, we could observe any bands in between 72 and 84 eV assigned to any Al species such as Al and Al_2O_3.[36,37] However, Al bands could not be observed in the wide energy range XPS spectra shown in Fig. S7 (ESI)† indicating that the electron-rich species of N and O are incorporated in the p-BN framework. Thus, the band at ~529.0 eV can be explained by the B–O–B species. Also, the bands at ~529.0 eV gradually increase with the increase of synthesis temperature meaning that B–OH species were converted to B–O–B species at the high temperature treatment. Such dehydration process reduces defective or chemically active sites to make p-BN more stable as shown in Fig. 3. Overall, these results suggest that adding elements, such as C and O, to the h-BN framework of p-BN produces locally electron-rich or chemically active species, which can explain the peculiar adsorption phenomena of p-BN.
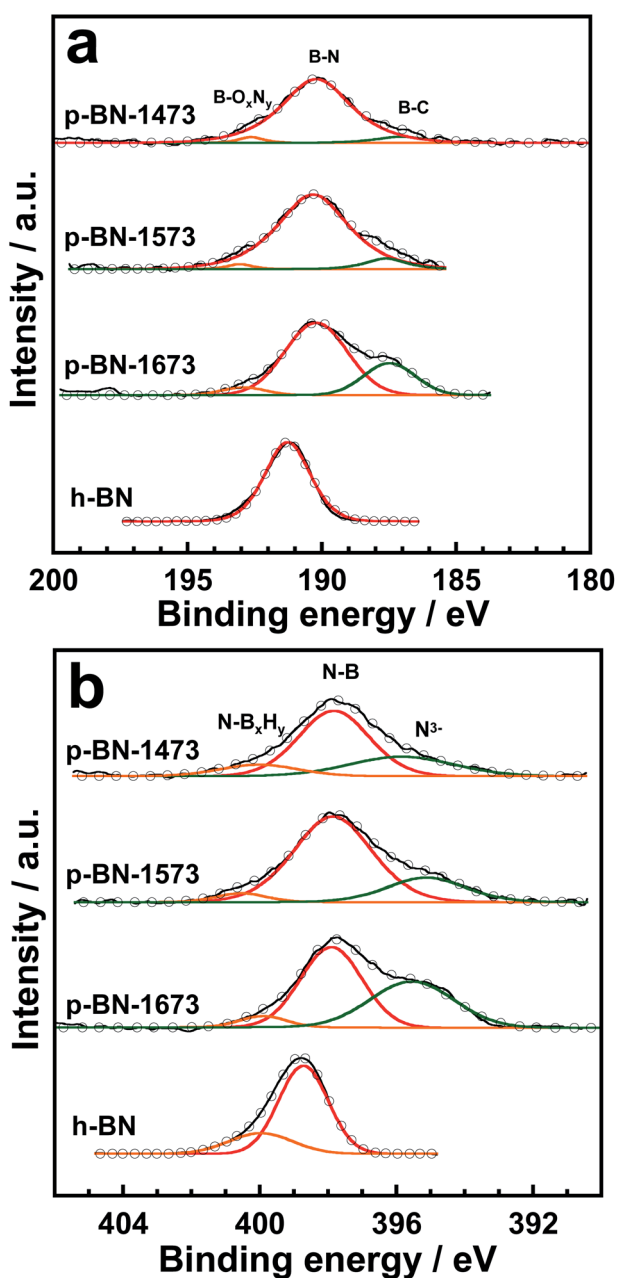
Gas adsorption ability of dinitrogen and argon on porous boron nitride

In this section, we discuss the adsorption ability of inactive gas molecules such as N_2 and Ar on p-BN. The boiling points of N_2 and Ar are 77 and 87 K, respectively, indicating that the interaction between Ar molecules is stronger than that between N_2 molecules. However, N_2 molecules have primitive quadrupole moments, which cause a weak interaction factor. The weak interaction is negligible, which indicates that N_2 is the most credible gas species for evaluating surface and pore parameters of solid materials. However, as per Wang et al., the PSD profile of a carbon material obtained by the N_2 adsorption isotherm shifts to a smaller size region than that obtained by the Ar adsorption isotherm, which can be attributed to adsorption enhancement due to the aforementioned weak interaction at the low-pressure region.[29] Therefore, if we compare adsorption isotherms between N_2 and Ar on p-BN, we can obtain some consequences for revealing the specific adsorption properties of N_2 to p-BN.

Fig. 5 shows the adsorption–desorption isotherms of N_2 on p-BN at 77 K. All isotherms are of type IV, indicating the

Fig. 4 XPS spectra of (a) B1s and (b) N1s of p-BN and h-BN. Here, black lines and circles denote experimental values and the sum of the components in the curve fitting procedure, respectively.

formation of micropores and mesopores.[28] All three isotherms are similar; negligible dependence of synthesis temperature to the adsorbed amount of N_2 can be observed. Table 1 summarizes the structural parameters obtained by α_s-plot analysis of the isotherms shown in Fig. 5.[38,39] The parameters of activated carbon (AC) obtained from the N_2 isotherms shown in Fig. S8 (ESI)† are also tabulated for comparison. Here, the isotherms of nonporous (*i.e.,* crystalline) h-BN were used as a standard data in the α_s-plot analysis. Consistent with Fig. 5, the micropore and mesopore parameters of p-BN are similar, the maximum deviation of which is roughly 10%. Similar to the average pore size of an AC named A7, the average micropore size of p-BN assuming a slit-shaped pore geometry is between 0.71 and 0.80 nm. The pore formation on p-BN can be supported by PSDs shown in Fig. S9 (ESI).† The results are almost consistent with those reported by Marchesini *et al.*[21] Thus, there is no doubt that both micropore and mesopore are constructed under high-temperature and N_2 gas flow conditions.

Before discussing Ar adsorption, the pore structure's stability for p-BN must be addressed because p-BN is more

Table 1 Pore-structure parameters of p-BN and AC obtained by α_s-plot analysis of N_2 adsorption isotherms at 77 K[a]

Sample	Micropore		Mesopore	
	V	a	V	a
p-BN-1473	0.377	1060	0.567	163
p-BN-1573	0.366	982	0.536	154
p-BN-1673	0.339	851	0.587	165
A7	0.151	493	0.007	8
A20	0.348	755	0.029	31

[a] The parameters are pore volume V/ml g^{-1} and specific surface area a/m^2 g^{-1}.

stable under high-temperature oxidation than typical carbon materials. As shown in Fig. S10 (ESI),† both micropore and mesopore structures of p-BN samples, except p-BN-1473, remain after the oxidation under atmospheric conditions at 973 K. Under atmospheric conditions, this excellent stability to heat treatment cannot be attained with carbon materials. On the one hand, the adsorption–desorption profile of p-BN-1473 after heat treatment is different than the one prior to heat treatment. Fig. 3, S3 and S4 (ESI)† show that the tendency coincides with stability. As per the XRD profiles shown in Fig. 1, every p-BN forms an amorphous structure, which can decrease the oxidation stability of p-BN, particularly p-BN-1473. However, as discussed using Fig. 4, additional heteroatomic species such as C and O are donated in the framework of h-BN microcrystals when p-BN is synthesized at higher temperatures. Although impregnated carbon species can decrease oxidation stability, the carbon deposited on the BN does not affect the oxidation process at temperatures of <1173 K.[40–42] Therefore, the oxidation stability of p-BN directly reflects the crystallinity of h-BN microcrystals.

Fig. 6 shows the adsorption–desorption isotherms of Ar on p-BN at 87 K. The deviation of Ar amount for adsorption branches on p-BN is considerably lesser than that of N_2 shown in Fig. 5; however, remarkable differences can be observed for the desorption branches in the Ar isotherms. The narrow deviation in the Ar adsorption isotherms in the region with low P/P_0 can be attributed to the nonexistence of specific interactions between Ar and p-BN surface. As per the analysis of Ar isotherms, pore parameters were obtained by the α_s-plot analysis, as shown in Table 2. The micropore and mesopore surface areas for p-BN obtained using Ar isotherms are lesser than those obtained using N_2 isotherms shown in Table 1. This can be attributed to the fact that specific interactions except the dispersion force do not occur between Ar and p-BN surface. On the other hand, the mesopore volumes obtained with Ar isotherms are larger than those obtained with N_2 isotherms; however, the difference in volume is <8%, which is small compared with all other differences except for the difference in micropore volume of p-BN-1673. Generally, the pore volume can be evaluated using the Gurvich rule,[28] in which the adsorbed density is assumed to be the liquid density of an adsorbate. Because the proportion of adsorbed molecules in direct contact
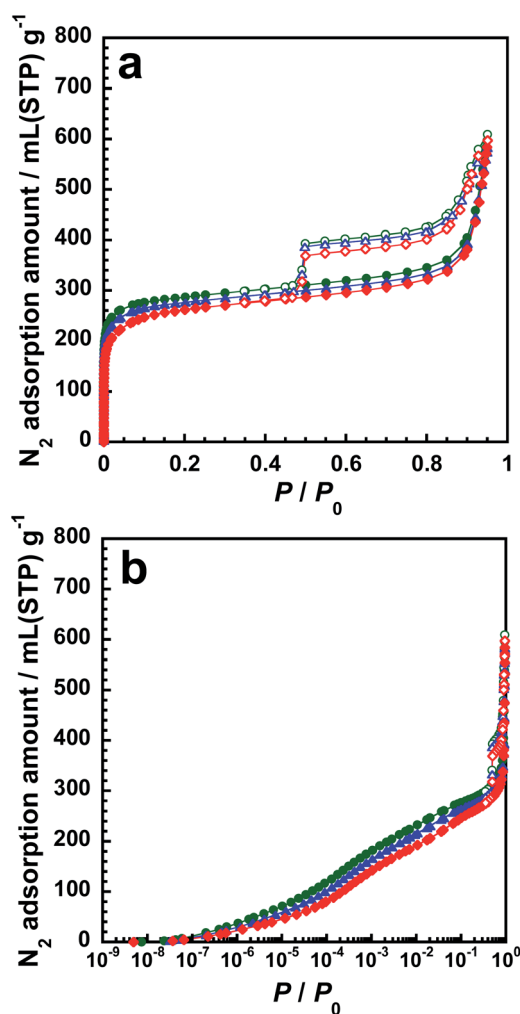

Fig. 5 Adsorption–desorption isotherms of N_2 at 77 K in (a) linear and (b) logarithmic scales on p-BN-1473 (green), p-BN-1573 (blue) and p-BN-1673 (red).

larger values for the mesopore volume. Hence, this result suggests that the pore surface of p-BN interacts with N_2 molecules more strongly than that of Ar, resulting in the enhancement of N_2 adsorption to p-BN.

Finally, we discuss a significant feature of N_2 adsorption on p-BN compared with Ar adsorption isotherms. An N_2 molecule typically interacts with other molecules or surfaces using the dispersion force and the weak interaction based on the quadrupole moment. Fig. 7 shows the relative adsorbed amount of N_2 as per that of Ar (denoted as V_{N2}/V_{Ar}) on p-BN and AC as functions of relative pressure in a logarithmic scale and the negative value of adsorption potential; *i.e.*, $-RT \ln(P_0/P)$. Here, both V_{N2} and V_{Ar} are the adsorbed volume at standard temperature and pressure per unit mass of the adsorbent. Hence, V_{N2}/V_{Ar} is the same as the molar ratio between adsorbed N_2 and Ar, *e.g.*, if $V_{N2}/V_{Ar} = 1$, the number of adsorbed N_2 molecules is the same as that of Ar molecules. First,
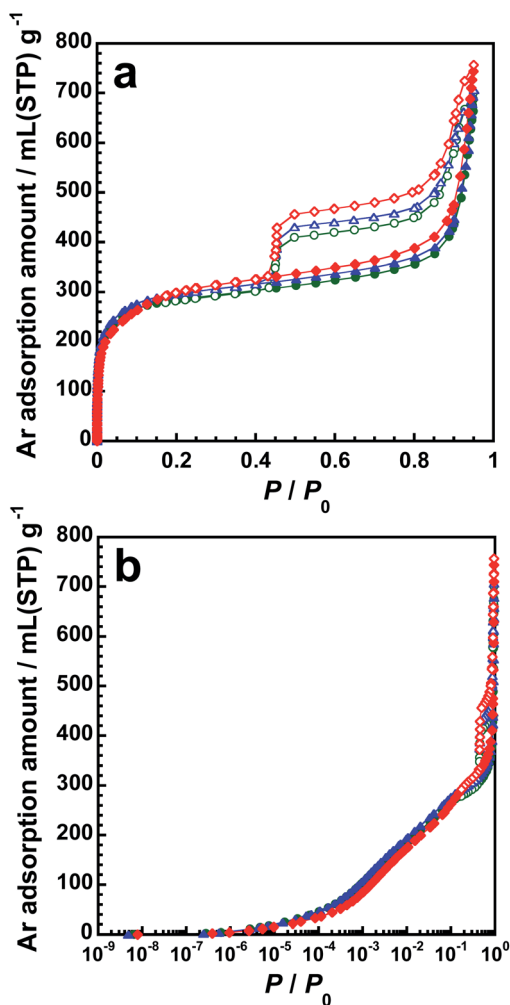

Fig. 6 Adsorption−desorption isotherms of Ar at 87 K in (a) linear and (b) logarithmic scales on p-BN-1473 (green), p-BN-1573 (blue) and p-BN-1673 (red).

Table 2 Pore-structure parameters of p-BN obtained by α_s-plot analysis of Ar adsorption isotherms at 87 K[a]

Sample	Micropore		Mesopore	
	V	a	V	a
p-BN-1473	0.316	886	0.579	130
p-BN-1573	0.330	898	0.571	134
p-BN-1673	0.333	782	0.633	151

[a] The parameters are pore volume V/ml g^{-1} and specific surface area a/m^2 g^{-1}.

with the mesopore surface to the total number of molecules confined in the mesopores is lesser compared with that of micropores, the mesopore volume is not affected by interactions between adsorbed molecules and surface but rather by the adsorbed density within the pore. Indeed, the molecular size of Ar is lesser than that of N_2; therefore, the closed-packed structure of Ar is well formed in the mesopores, which results in the
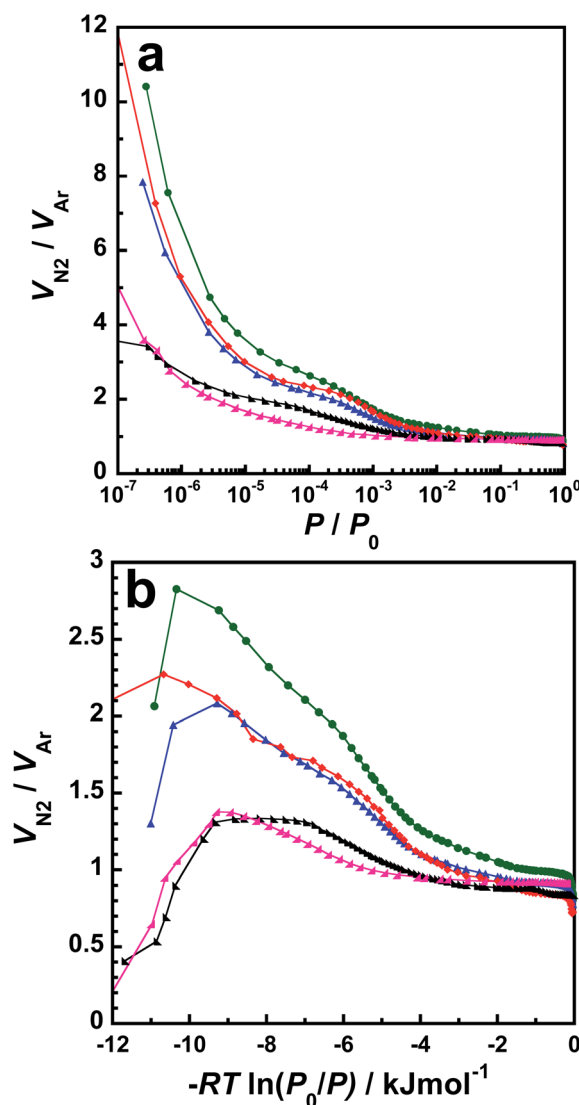

Fig. 7 Relative adsorption amounts of N_2 to Ar on p-BN-1473 (green), p-BN-1573 (blue), p-BN-1673 (red) and AC of A7 (pink) and A20 (black). Here, the horizontal axes are (a) relative pressure and (b) negative value of adsorption potential.

every relative adsorbed amount of N_2 on p-BN is evidently larger than that of AC, as shown in Fig. 7a and b, which supports the idea that stronger interaction occurs between an N_2 and the p-BN surface compared with that of AC. For instance, the maximum V_{N_2}/V_{Ar} value for A7 is 1.38 at $-RT \ln(P_0/P) = -9.28$ kJ mol^{-1} where $V_{N_2}/V_{Ar} = 2.69$ for p-BN-1473 at the same adsorption potential. These values show that twice the number of N_2 molecules can be restricted in the pore of p-BN-1473 than in the pore of A7 when the data are normalized by adsorbed amounts of Ar. Furthermore, the p-BN profiles strongly depend on the synthesis temperature; however, the A7 profile in Fig. 7a and b is similar to that of A20, which suggests similar interaction and filling processes for AC. Focusing on p-BN profiles, every profile of relative adsorbed amount of N_2 shown in Fig. 7a involves the following two features: (1) steep uptake of less than $P/P_0 = 10^{-5}$ and (2) approaching unity at higher relative pressure regions. The steep gradient in the low-pressure region is attributed to the strong interaction between an N_2 molecule and the pore wall of p-BN, which indicates that N_2 molecules tend to form stable adsorbed phases when attached to the surface at the low-pressure region. A similar tendency can be observed at over -8 kJ mol^{-1} in Fig. 7b. Moreover, the low-pressure and low $-RT \ln(P_0/P)$ regions of p-BN-1473 considerably vary. This is because, out of all the samples, p-BN-1473 has the largest number of chemically active sites, which act as adsorption sites for N_2. This hypothesis can then be supported by the stability order discussed in the previous section; *i.e.*, p-BN-1473 is the most unstable adsorbent with respect to oxidation under atmospheric conditions, although it has a small number of heteroatoms involving C and O. Here, the active sites do not form any bonds with N_2 molecules since it is one of the most stable species. In fact, the structure of p-BN even after the N_2 adsorption experiment was the same as its initial one even for p-BN-1473 as evidenced by XRD profiles, scanning electron microscopy (SEM) images and IR spectra shown in Fig. S11–S13 (ESI),† respectively. The results support that an additional physical interaction between a N_2 molecule and the p-BN surface enhances the N_2 adsorption. The impregnation of C and O species does not affect the stability of p-BN against the oxidation but reduces the number of chemically active sites for N_2 adsorption. For p-BN-1673, a convex profile can be observed between $P/P_0 = 10^{-4}$ and 10^{-3} in Fig. 7a and between $-RT \ln(P_0/P) = -6$ and -4 kJ mol^{-1} in Fig. 7b. As shown in Fig. S14 (ESI),† this can be observed in the same plot for h-BN. The convex profile suggests adsorption enhancement to N_2. A possible reason for the upper deviation is the formation of a stable adsorbed layer attached to the surface of p-BN-1673 and h-BN. As shown in Fig. 1, the microcrystal in the p-BN-1673 forms the most ordered structure of all p-BN samples; however, p-BN crystallinity is still low compared with that of h-BN. Hence, adsorbed molecules can form a relatively uniform adsorbed layer in the vicinity of the basal plane surface of the h-BN crystallite. If the interaction between the adsorbed molecule and the surface is significant, the surface will enhance the uniform formation of the adsorbed layer. At the juncture before the perfect formation of the first adsorbed layer of N_2, voids are created around the adsorbed molecules in the adsorbed layer, which, in turn, enhances additional N_2 adsorption. As discussed, the interaction between N_2 and the surface of p-BN is stronger than that of Ar; therefore, a characteristic profile in the

relative adsorption amount of N_2 for p-BN-1673 is observed because of the uniform adsorbed layer formation of N_2. Moreover, N_2 adsorption is enhanced because of adsorption sites formed by heteroatomic species impregnated into the h-BN microcrystal of p-BN-1673. Because partially electron-rich sites were introduced by impregnation of hetero atoms, as shown by XPS spectra, certain active sites work as specific sites for N_2 adsorption. However, additional supporting evidence is required to discuss this phenomenon. Based on the information obtained from our current study, it is evident that the p-BN profiles are attributed to (1) different characteristic formation of the adsorbed phase of N_2 within the pores of p-BN compared with that within the pores of AC and/or (2) the existence of specific interactions between an N_2 molecule and the p-BN surface with chemically specific sites created by C and/or O impregnation.

The results of the gas adsorption experiments suggest that N_2 adsorption is enhanced by the strong interaction between an N_2 molecule and the p-BN surface because of a characteristic surface of p-BN micropore and active sites impregnated in the microcrystals. Although the specific interaction initiated by p-BN must be immediately elucidated, p-BN can be an unparalleled adsorbent with strong interaction sites for various molecules.

Conclusions

In this study, p-BN with h-BN pore walls was synthesized by high-temperature calcination. The results suggest that N_2 molecules strongly interact with the p-BN surface according to the p-BN structure. The synthesis method involved high-temperature treatment under an N_2 flow condition; it provided appropriate surface conditions for N_2 adsorption. The adsorption features were different compared with typical porous carbon materials. Moreover, although hetero-atomic species, such as C and O, are more impregnated in the p-BN framework when treated at higher temperatures, the crystallinity of p-BN strengthens the oxidation stability up to 973 K under atmospheric conditions. Furthermore, although the p-BN frameworks were similar to h-BN frameworks, the stability, surface chemistry, and adsorption properties to N_2 were dependent on the treatment temperature required to yield p-BN. The molecular number of adsorbed N_2 on p-BN was ~150%–200% larger than that on AC at the same adsorption potential state when we compared the amount normalized by the adsorbed amount of Ar. Thus, the excellent oxidation stability and specific adsorption nature of p-BN suggests that it is a novel adsorbent and catalyst.

Experimental

Synthesis of porous boron nitride

The p-BN samples were synthesized as per a template-free method reported by Marchesini *et al.*[21] In essence, boric acid (120 mg, purity of 99.5%, FUJIFILM Wako Pure Chemical Co.) and urea (580 mg, purity of 99.0%, FUJIFILM Wako Pure Chemical Co.) were mixed with an agate mortar for 15 min. The homogeneously mixed powder sample in an alumina boat was

Paper

then placed into a horizontal alumina tube; N_2 was then introduced by an appropriate flow process (150 ml min^{-1} for 2 h). The sample was then calcined at temperatures of 1473, 1573, and 1673 K under N_2 gas flow (50 ml min^{-1}) for 3 h. For each temperature, the heating rate was 10 K min^{-1}. The synthesized sample was denoted as p-BN-x where x is the maximum temperature of the calcination process.

Activated carbon

Pitch-based AC fibres (A7 and A20 produced by AD'ALL Co. Ltd.) were used. These carbon materials have a large amount of micropores; the average sizes of which is ~0.7 nm for A7 and ~1.0 nm for A20.[43]

Characterization

The XRD profile for each sample was collected using MiniFlexII (Rigaku Co. Ltd.) at room temperature. Monochromatic X-rays of Cu Kα radiation ($\lambda = 0.154$ nm) at 30 kV and 15 mA was applied. The observations of HR-TEM and STEM images were collected by ARM-200CF (JEOL, Ltd.) at an accelerated voltage of 120 kV. The sample was dispersed in highly purified hexane followed by dropping on a Cu mesh covered with carbon membranes (NS-C15, Okenshoji Co., Ltd.). TG profiles were obtained using Thermo plus EVO2 (Rigaku Co. Ltd.) under atmospheric conditions. In a typical TG experiment, ~4 mg of a sample was placed in a Pt pan, and measurements were performed at a ramping rate of 10 K min^{-1} from room temperature to 1173 K. Moreover, XPS measurements were conducted using JEOL JPS-9030. The spectra were analysed with JEOL SpecSurf systems to deconvolute and analyse the bands. N_2 adsorption–desorption isotherms at 77 K and Ar isotherms at 87 K on p-BN and AC were then measured using BELSORP-max (Micro-tracBEL Corp.), and all samples were evacuated at 823 K at <1 mPa for 6 h.

Conflicts of interest

There are no conflicts to declare.

Acknowledgements

References

1 S. Iijima, *Nature*, 1991, **354**, 56–58.

2 S. Iijima and T. Ichihashi, *Nature*, 1993, **363**, 603–605.

3 R. M. Barrer, *Zeolites and clay minerals as sorbents and molecular sieves*, Academic Press, New York, 1978.

4 S. R. Batten and R. Robson, *Angew. Chem., Int. Ed.*, 1998, **37**, 1460–1494.

5 D. Li and K. Kaneko, *Chem. Phys. Lett.*, 2001, **335**, 50–56.

6 B. Moulton and M. Zawartko, *Chem. Rev.*, 2001, **101**, 1629–1658.

7 O. M. Yaghi, M. O'Keeffe, N. W. Ockwig, H. K. Chae, M. Eddaoudi and J. Kim, *Nature*, 2003, **423**, 705–714.

8 A. Kondo, T. Yashiro, N. Okada, S. Hiraide, T. Ohkubo, H. Tanaka and K. Maeda, *J. Mater. Chem. A*, 2018, **6**, 5910–5918.

9 T.-A. Chen, C.-P. Chuu, C.-C. Tseng, C.-K. Wen, H.-S. P. Wong, S. Pan, R. Li, T.-A. Chao, W.-C. Chueh, Y. Zhang, Q. Fu, B. I. Yakobson, W.-H. Chang and L.-J. Li, *Nature*, 2020, **579**, 219–223.

10 S. Hong, C.-S. Lee, M.-H. Lee, Y. Lee, K. Y. Ma, G. Kim, S. I. Yoon, K. Ihm, K.-J. Kim, T. J. Shin, S. W. Kim, E. Jeon, H. Jeon, J.-Y. Kim, H. Lee, Z. Lee, A. Antidormi, S. Roche, M. Chhowalla, H.-J. Shin and H. S. Shin, *Nature*, 2020, **582**, 511–514.

11 J. T. Grant, C. A. Carrero, F. Goeltl, J. Venegas, P. Muller, S. P. Burt, S. E. Specht, W. P. McDermott, A. Chieregato and I. Hermans, *Science*, 2016, **354**, 1570–1573.

12 J. Tian, J. Tan, M. Xu, Z. Zhang, S. Wan, S. Wang, J. Lin and Y. Wang, *Sci. Adv.*, 2019, **5**, eaav8063.

13 M. Terrones, W. K. Hsu, H. Terrones, J. P. Zhang, S. Ramos, J. P. Hare, R. Castillo, K. Prassides, A. K. Cheetham, H. W. Kroto and D. R. M. Walton, *Chem. Phys. Lett.*, 1996, **259**, 568–573.

14 C. Tang, Y. Bando, T. Sato and K. Kurashima, *Chem. Commun.*, 2002, 1290–1291.

15 S. Frueh, R. Kellett, C. Mallery, T. Molter, W. S. Willis, C. King'ondu and S. L. Suib, *Inorg. Chem.*, 2011, **50**, 783–792.

16 W.-Q. Han, R. Brutchey, T. D. Tilley and A. Zettl, *Nano Lett.*, 2004, **4**, 173–176.

17 T. Oku, M. Kuno and I. Narita, *J. Phys. Chem. Solids*, 2004, **65**, 549–552.

18 B. Rushton and R. Mokaya, *J. Mater. Chem.*, 2008, **18**, 235–241.

19 S. Schlienger, J. Alauzun, F. Michaux, L. Vidal, J. Parmentier, C. Gervais, F. Babonneau, S. Bernard, P. Miele and J. B. Parra, *Chem. Mater.*, 2012, **24**, 88–96.

20 Q. Weng, X. Wang, C. Zhi, Y. Bando and D. Golberg, *ACS Nano*, 2013, **7**, 1558–1565.

21 S. Marchesini, C. M. McGilvery, J. Bailey and C. Petit, *ACS Nano*, 2017, **11**, 10003–10011.

22 D. Saha, G. Orkoulas, S. Yohannan, H. C. Ho, E. Cakmak, J. Chen and S. Ozcan, *ACS Appl. Mater. Interfaces*, 2017, **9**, 14506–14517.

23 S. Marchesini, A. Regoutz, D. Payne and C. Petit, *Micropor. Mesopor. Mater.*, 2017, **243**, 154–163.

24 R. Shankar, S. Marchesini and C. Petit, *J. Phys. Chem. C*, 2019, **123**, 4282–4290.

25 R. Shankar, M. Sachs, L. Francàs, D. Lubert-Perquel, G. Kerherve, A. Regoutz and C. Petit, *J. Mater. Chem. A*, 2019, **7**, 23931–23940.

26 A. V. Neimark, P. I. Ravikovitch, M. Grun, F. Schuth and K. K. Unger, *J. Colloid Interface Sci.*, 1998, **207**, 159–169.

27 S. Lowell, J. E. Shields, M. A. Thomas and M. Thommes, *Characterization of porous solids and powders: surface area, pore size and density*, Kluwer Academic Publishers, 2004.

28 M. Thommes, K. Kaneko, A. V. Neimark, J. P. Olivier, F. Rodriguez-Reinoso, J. Rouquerol and K. S. W. Sing, *Pure Appl. Chem.*, 2015, **87**, 1051–1069.

29 S. Wang, D. Minami and K. Kaneko, *Micropor. Mesopor. Mater.*, 2015, **209**, 72–78.

30 T. Ohkubo, T. Iiyama, K. Nishikawa, T. Suzuki and K. Kaneko, *J. Phys. Chem. B*, 1999, **103**, 1859–1863.

31 R. Geick and C. H. Perry, *Phys. Rev.*, 1966, **146**, 543–547.

32 A. Prakash and K. B. Sundaram, *Appl. Surf. Sci.*, 2017, **396**, 484–491.

33 S. Meskinis, M. Mndrulevicius, V. Kopustinskas and S. Tamulevicius, *Appl. Surf. Sci.*, 2005, **249**, 295–302.

34 M. Wang, Y. Bai, B. Zhang, B. Zhong, Y. Yu, J. Zhang, X. Huang and G. Wen, *Ceram. Int.*, 2019, **45**, 6684–6692.

35 R. Ramachandran, D. Jung, N. A. Bernier, J. K. Logan, M. A. Waddington and A. M. Spokoyny, *Inorg. Chem.*, 2018, **57**, 8037–8041.

36 P. Hirchenhahn, A. Al Sayyad, J. Bardon, A. Felten, P. Plapper and L. Houssiau, *ACS Appl. Polym. Mater.*, 2020, **2**, 2517–2527.

37 K. H. Maria, P. Sultana and M. B. Asfia, *AIP Adv.*, 2020, **10**, 065315, 10 pp.

38 K. Kaneko and C. Ishii, *Colloids Surf.*, 1992, **67**, 203–212.

39 N. Setoyama, T. Suzuki and K. Kaneko, *Carbon*, 1998, **36**, 1459–1467.

40 F. Guo, P. Yang, Z. Pan, X. Cao, Z. Xie and X. Wang, *Angew. Chem., Int. Ed.*, 2017, **56**, 8231–8235.

41 S. Chen, P. Li, S. Xu, X. Pan, Q. Fu and X. Bao, *J. Mater. Chem. A*, 2018, **6**, 1832–1839.

42 M. Florent and T. J. Bandosz, *J. Mater. Chem. A*, 2018, **6**, 3510–3521.

43 T. Ohkubo, M. Nishi and Y. Kuroda, *J. Phys. Chem. C*, 2011, **115**, 14954–14959.